Journal of
Micro/Nanolithography,
MEMS, and MOEMS

Nanolithography.SPIEDigitalLibrary.org

Pattern inspection of etched multilayer extreme ultraviolet mask

Susumu Iida
Ryoichi Hirano
Tsuyoshi Amano
Hidehiro Watanabe

SPIE.

Pattern inspection of etched multilayer extreme ultraviolet mask

Susumu Iida,* Ryoichi Hirano, Tsuyoshi Amano, and Hidehiro Watanabe
EUVL Infrastructure Development Center Inc., 16-1 Onogawa, Tsukuba-shi, Ibaraki-ken 305-8569, Japan

Abstract. Patterned mask inspection for an etched multilayer (ML) extreme ultraviolet mask was investigated. In order to optimize the mask structure from the standpoint of a pattern inspection the mask structure not only from the standpoint of a pattern inspection by using a projection electron microscope but also by using a projection electron microscope but also by considering the other fabrication processes using electron beam techniques such as critical dimension metrology and mask repair, we employed a conductive layer between the ML and substrate. By measuring the secondary electron emission coefficients of the candidate materials for the conductive layer, we evaluated the image contrast and the influence of the charging effect. In the cases of 40-pair ML, 16-nm-sized extrusion and intrusion defects were found to be detectable more than 10 sigma in half pitch 44, 40, and 32 nm line-and-space patterns. Reducing 40-pair ML to 20-pair ML degraded the image contrast and the defect detectability. However, by selecting B_4C as a conductive layer, 16-nm-sized defects and etching residues remained detectable. The 16-nm-sized defects were also detected after the etched part was refilled with Si. A double-layer structure with 2.5-nm-thick B_4C on metal film used as a conductive layer was found to have sufficient conductivity and also was found to be free from the surface charging effect and influence of native oxide. [DOI: 10.1117/1.JMM.15.2.021002]

Keywords: extreme ultraviolet mask; high numerical aperture; defect detection; pattern inspection; Monte Carlo simulation; projection electron microscope.

Paper 15145SSP received Sep. 25, 2015; accepted for publication Jan. 5, 2016; published online Jan. 29, 2016.

1 Introduction

Extreme ultraviolet (EUV) lithography is the most advanced lithographic technology to fabricate 1× nm node devices. Pattern size shrinkage to ∼10 nm requires an exposure tool with a higher numerical aperture (NA), and the high NA leads to an increase in the chief ray angle (CRA) of EUV light as shown in Fig. 1(a).[1] As a result, mask three-dimensional effects, such as the shadowing effect, become larger with a conventional stacked absorber-type EUV mask structure [Fig. 1(b)],[2] and thus, the lithography process margin decreases. Recently, Kamo et al. proposed that the binary etched multilayer (ML) mask is very effective to overcome this issue as shown in Fig. 1(c).[3–6]

Moreover, Kim et al. also confirmed this observation by numerical analysis.[7,8] However, the mask structure should be taken into account when dealing with the mask fabrication processes, such as patterned mask inspection,[9–13] critical dimension measurement (CD metrology),[14,15] mask repair,[16,17] and cleaning.[18] Takai et al. reported that the reduction of the ML stack down to 20 pairs effectively avoided the collapse of the lines by the cleaning process.[19] However, patterned mask inspection, CD metrology, and repair of this mask structure continue to pose challenges that need to be addressed. In these processes, electron beam (EB) techniques are often used; therefore, charging effects tend to cause some degradation of process accuracy. Takai et al. also reported that a conductive layer between the SiO_2 substrate [or some low thermal expansion material (LTEM)] and ML was effective to avoid an electrical floating of the EUV mask inside a black border of etched ML. With this approach, the EB image quality of the mask was effectively improved.[20] As a result, the repeatability of metrology and the sensitivity of inspection for this type of EUV mask were also improved.[20] However, the optimization of the material and structure of the conductive layer is critical, because this issue should be studied with taking into account the conductivity, durability for cleaning, oxidization, roughness, and etching selectivity of the material and the impact on the image contrast. We have learned that the image contrast is determined by the secondary electron emission coefficients (SEECs) of materials that the EUV mask is composed of and by the geometries involved. They also influence the defect detection sensitivity of a projection electron microscope (PEM) inspection system.[21–25] The PEM has the advantage of a much higher throughput than what is achievable in the case of a conventional scanning electron microscope (SEM) type inspection system.[9,11–13,21–26] That is because PEM probes a sample target with large field illumination, whereas SEM probes a sample with a spot beam. In this paper, we investigated the defect detectability of etched ML-EUV masks, and we propose a better and more feasible structure, which would improve the processing accuracy in working with EB systems.

2 Experimental

Candidate materials to serve as the conductive layers were selected among the familiar materials used in photomasks. TaN, Ru, CrN, TiN, and Si are materials commonly used in EUV and conventional photomasks. B_4C is also widely studied as an interdiffusion barrier between Mo and Si for EUV reflective ML mirrors,[27] and as a capping layer of the

*Address all correspondence to: Susumu Iida, E-mail: susumu.iida@eidec.co.jp

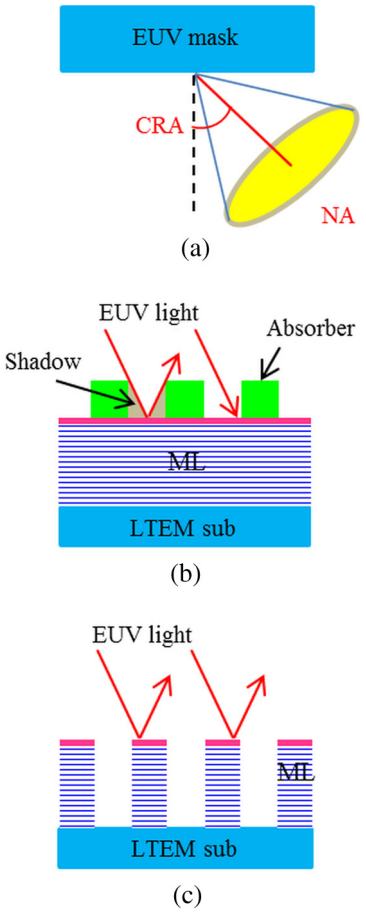

Fig. 1 Schematic explanations of (a) relationship between CRA and high-NA exposure, (b) shadowing effect of conventional EUV mask, and (c) etched ML-EUV mask.

ML.[28] In order to evaluate the PEM image contrast of a line-and-space (L/S) pattern, the SEECs of these materials with 100 nm thickness deposited on quartz substrates were measured using a specially designed scanning Auger microscope.[29] It should be noted that the obtained data were measured in as-is (as-deposited) conditions, with their native oxide films on their surface, in order to demonstrate the actual mask surface condition. The electrical resistivities of these films were measured by a four-point probe method with 0.3 mm spacings between the neighboring probes. In order to evaluate the defect detection sensitivity of a PEM inspection system, simulated PEM images were obtained using a CHARIOT Monte Carlo software (Abeam Technologies Inc.).[30] The simulated PEM images take into account the characteristics of electron imaging optics, such as their aberrations, electron transmittance, and aperture stops, because these images are obtained at a conjugate image plane of the real application.[25,26] For these simulations, the illumination and imaging system used were originally designed with an inspection capability for pattern sizes as narrow as half pitch (hp) 64 nm.[26] Moreover, this system design allows the detection of defect sizes as small as 16 nm (on mask).[26] Thus, based on the defect signal intensity of 16-nm-sized defects, the defect detectability in etched ML-EUV masks (of various structures) were evaluated and compared. The MLs consist of 20 and 40 pairs of 3-nm-thick Mo and 4-nm-thick Si with a 2.5-nm-thick Ru capping layer. The hp 44 to 32 nm L/S patterns on mask (corresponding to hp 11 to 8 nm technology on wafer) were utilized in anticipation of pattern sizes at high-NA exposure.[1,2] A detailed method of simulated PEM image acquisition is described elsewhere.[25,26] In order to improve the reliability of the simulation results, the SEECs of the utilized materials were employed for the calibration of the simulation results. The difference between the simulated PEM image with defects and that without defects is defined as the difference image. In order to define the sensitivity of defect detection, we identified the signal intensity in the difference image with more than 10 times the intensity of the standard deviation of the background intensity levels as a defect (10σ). Image processing operations were applied to the simulated image to enhance the to enhance the defect signal intensities.[22,31] The image contrast of the L/S pattern is expressed as a modulation transfer function (MTF), defined as [(maximum value − minimum value)/(maximum value + minimum value)].

3 Results and Discussion

3.1 *Analysis of the Secondary Electron Emission Coefficients of Utilized Materials and Their Impacts on Projection Electron Microscope Image Contrast*

Figure 2(a) shows the experimentally obtained SEECs of TaN, CrN, TiN, Si, B_4C films, and Ru-capped ML. The SEEC curves of CrN and TiN are almost identical, and the overall SEECs of B_4C is the lowest among all these materials. These results make sense because the SEEC increases with the atomic number Z in general.[32] We have learned that the SEEC difference between lines and spaces determines the gray level difference of the captured images corresponding to the material contrasts.[22,24,25] As shown in Fig. 2(b), the SEEC difference between ML and B_4C turns out to be the largest. In the case of TaN, the SEEC difference shows a negative value because the SEECs of TaN is larger than those of ML. This result indicates that the combination of Ru-capped ML and TaN exhibits the image contrast reversal as compared with the other materials.

The image contrast is also affected by the sample geometry. Especially for the etched ML mask, the aspect ratio of the L/S pattern is considerably high, as shown in Fig. 3.

The secondary electrons (SEs) generated from the bottom of the space are blocked by the sidewalls of the lines. Therefore, the SE signals from the space decrease as the aspect ratio becomes high.[13,22,24,33] Hence, this effect enhances the L/S pattern image contrast when the SEEC of the space material (conductive layer) is lower than that of ML.

Figure 4 shows the apparent SEEC and SEEC difference change of a high aspect ratio pattern on the Si layer. SEEC itself is one of the physical constants. However, a decrease in the SE signals from the bottom of the space can be considered as an apparent SEEC decrease for a better understanding of the phenomenon. As the percentage of the SE signals from the bottom decreases, the apparent SEEC becomes low as shown in Fig. 4(a); while the apparent SEEC difference between ML and Si increases, and the peak of the curve is shifted to the lower incident beam energy as shown in Fig. 4(b). These results indicate that as the aspect ratio becomes high, the optimal incident beam energy to obtain the highest image contrast becomes low. Furthermore, when

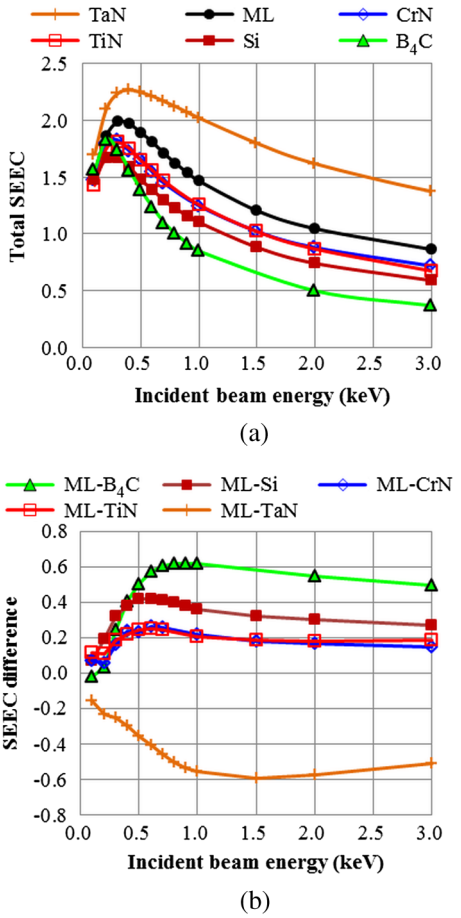

Fig. 2 (a) Experimentally obtained SEECs of 100-nm-thick TaN, CrN, TiN, Si, B_4C films, and Ru-capped ML, and (b) their experimental SEEC difference (which was calculated by subtracting SEECs of these thin films from that of the Ru-capped ML), as functions of incident beam energy. All the materials were measured in as-is conditions.

the SE signal from the bottom is extremely low (1%), the SEEC difference curve becomes identical to the SEEC curve of ML. As a result, the optimal condition is determined by the peak of the ML. This result is in good agreement with our previous work for the investigation of the optimal incident beam energy to detect the small intrusion defect.[22,24] In order to confirm the impact of the conductive layer on the image contrast, simulated PEM images were obtained using a sample structure with an hp 40 nm L/S pattern in 40-pair-ML on various conductive layers as shown in Fig. 5. Incident beam energy of 300 eV creates the most sensitive condition for defect detection in this sample geometry. In the case of Ru, the L/S pattern is hardly identifiable in spite of the high aspect ratio of 7.2 because the material contrast between Ru-capped ML and Ru conductive layer is very low.[23] Moreover, the MTF of the TaN sample is lower than that of the Ru one because the higher SEEC of TaN cancels out the effect of a high aspect ratio.

On the other hand, by reducing 40-pair ML to 20-pair ML, the MTF value of the TaN sample increases, and the contrast of the L/S pattern is reversed as compared with the CrN, Si, and B_4C samples as shown in Fig. 6. These image contrasts correspond to their material contrasts derived from the SEEC curves as shown in Fig. 2. Furthermore, the MTF values of Si and B_4C show a significant difference for the case with 20-pair ML (0.22 and 0.25, respectively), whereas the values for the case with 40-pair ML are about the same (0.26 and 0.25, respectively). These results indicate that the conductive layer underlying 20-pair ML has a greater impact on the EB image contrast than in the case of 40-pair ML and that the B_4C sample has the highest image contrast of the L/S pattern. It is also noted that the optimal incident beam energy for defect detection in the geometry of 20-pair-ML is higher than that of the 40-pair ML, due to an increase in the percentage of the detectable SEs from the conductive layer as shown in Fig. 4(b).

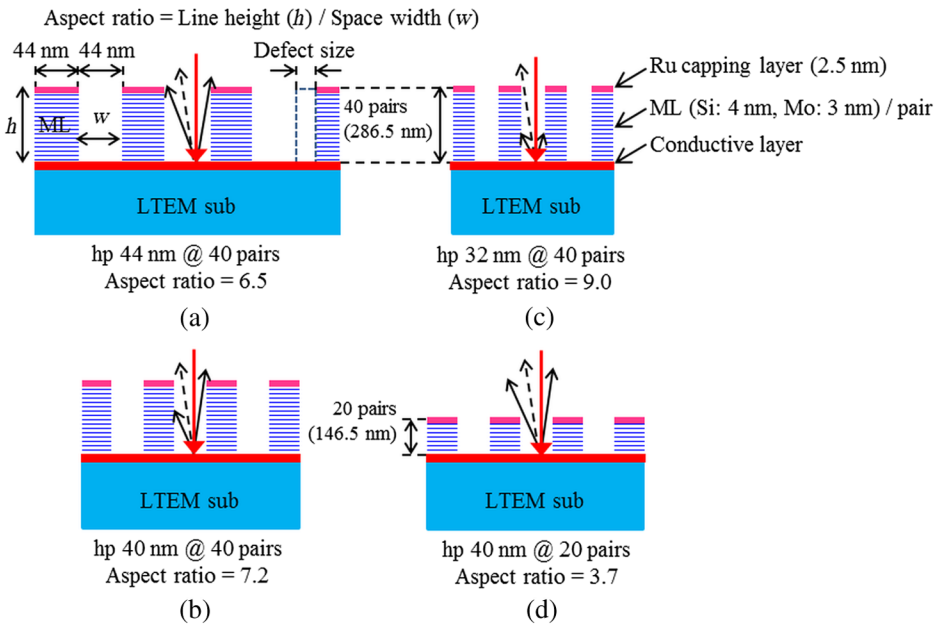

Fig. 3 Schematic illustrations of SEs from the bottom of the etched ML mask with hp (a) 44 nm, (b) 40 nm, and (c) 32 nm L/S patterns in 40-pair ML, and (d) 40 nm L/S pattern in 20-pair ML. The aspect ratios of the L/S patterns are 6.5, 7.2, 9.0, and 3.7, respectively.

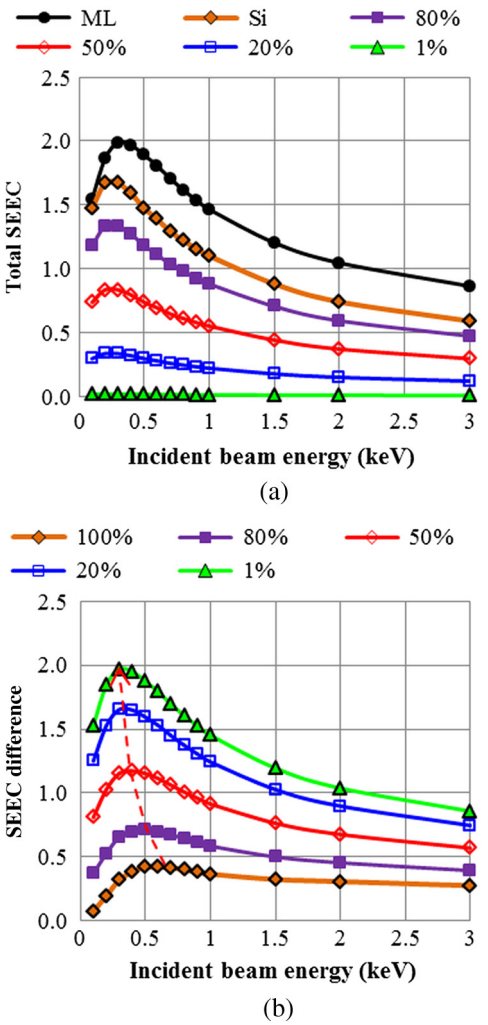

Fig. 4 Apparent (a) SEEC and (b) SEEC difference change of high aspect ratio patterns on the Si layer. The graph legend "1%" means that only 1% of the total electrons emitted reach the detector. This is because 99% of electrons emitted from the bottom of the trench are blocked by the pattern sidewalls. By the same principle, the graph legend "100%" means that all the SEs reach the detector without any obstruction by the pattern sidewalls.

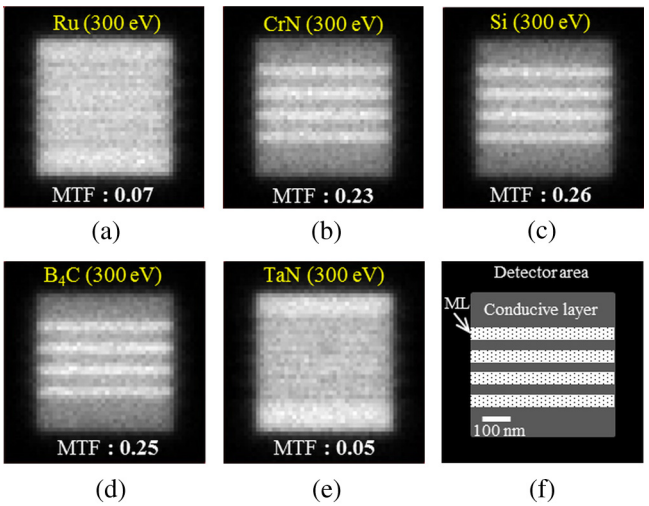

Fig. 5 Simulated PEM image of etched 40-pair-ML EUV mask with hp 40 nm L/S pattern on the conductive layers of (a) Ru, (b) CrN or TiN, (c) Si, (d) B_4C, (e) TaN, and (f) their schematic illustration. Incident beam energy and MTF of L/S pattern are shown on the upper and lower parts of the image.

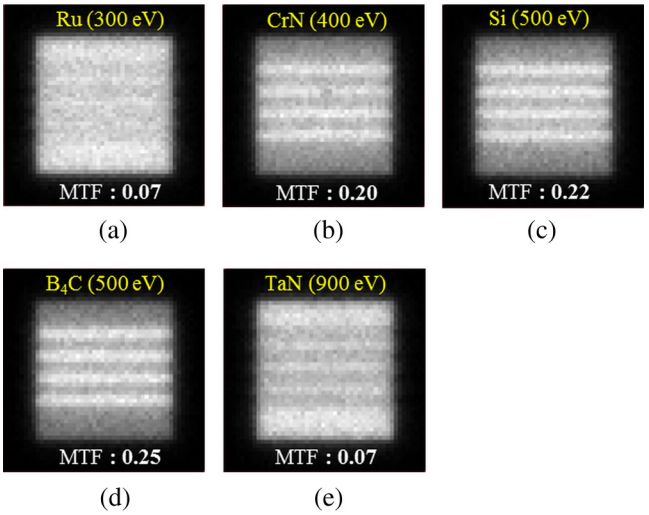

Fig. 6 Simulated PEM image of etched 20-pair-ML EUV mask with hp 40 nm L/S pattern on the conductive layers of (a) Ru, (b) CrN or TiN, (c) Si, (d) B_4C, and (e) TaN. Incident beam energy and MTF of the L/S pattern are shown on the upper and lower parts of the image.

3.2 *Investigation of the Impact of Aspect Ratio and Conductive Layer on Defect Detectability*

In order to investigate the impact of the aspect ratio and conductive layer on the defect detectability of a PEM inspection system for etched ML-EUV masks, a die-to-die inspection is demonstrated using simulated PEM images with and without defects. Figure 7 shows the difference images for the cases of a 40-pair ML on an Si layer. A set of extrusion and intrusion defects with 22 and 16 nm sizes are detected more than 10σ in all the cases of hp 44, 40, and 32 nm L/S patterns. As shown in Figs. 3(a)–3(c), their aspect ratios are 6.5, 7.2, and 9.0, respectively. The illumination and the imaging systems used for this simulation are designed for an hp 64 nm L/S pattern (hp 16 nm on wafer). Therefore the spatial resolution is not sufficient for smaller hp L/S patterns, such as less than hp 40 nm (hp 10 nm on wafer). Thus, the defect detection sensitivity degrades along with the pattern size shrink in spite of the increase of aspect ratio. We have learned that the spatial resolution has a great impact on the defect detectability, especially for small defects.[13] In order to increase the detectability, the spatial resolution needs to be improved, and we are now developing a new PEM inspection system designed for 11 nm node.[34]

Figure 8 shows the difference images for the cases of 20-pair ML with an hp 40 nm L/S pattern on various conduction layers. By reducing 40-pair ML to 20-pair ML, 16-nm-sized extrusion defects on the Si layer become undetectable. Only in the case of the B_4C sample, 16-nm-sized extrusion defects are detected more than 10σ. These results indicate that the selection of a conductive layer with higher material contrast is critical for high sensitivity pattern inspection of an etched 20-pair ML EUV mask. In order to confirm the threshold level for defect detection, the difference images with various threshold levels are shown in Fig. 9. In the case of 5σ, a 16 nm extrusion defect is detected even on Si, but

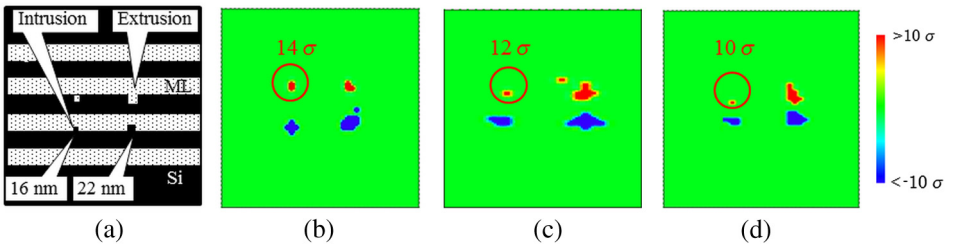

Fig. 7 (a) Top view of the schematic illustration of etched 40-pair-ML EUV mask with defects, and simulated difference images of (b) hp 44, (c) hp 40, and (d) hp 32 nm L/S patterns on the conductive layer of Si.

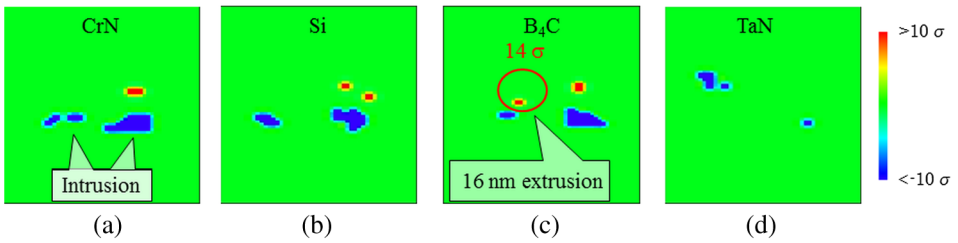

Fig. 8 Simulated difference images using etched 20-pair-ML EUV mask with hp 40 nm L/S pattern on the conductive layers of (a) CrN or TiN, (b) Si, (c) B_4C, and (d) TaN.

some false defects are also observed in all samples. On increasing the threshold, the false defects decrease, and then, in the case of 10σ, a 16-nm-sized extrusion defect is detected without any false defects on the B_4C sample. This result indicates that 10σ is the required condition for inspection without false defects.

In order to prevent any oxidation of the etched part, several researchers proposed that the etched part be replaced by other materials as shown in Fig. 10.[7] In this study, Si is filled up to the same level as the Ru capping layer. In this case also, 16- and 22-nm-sized extrusion and intrusion defects are detected.

It is to be noted that the optimal incident beam energy (600 eV) is different from the case of the as-etched (before Si is filled with the etched part) mask (500 eV). This energy

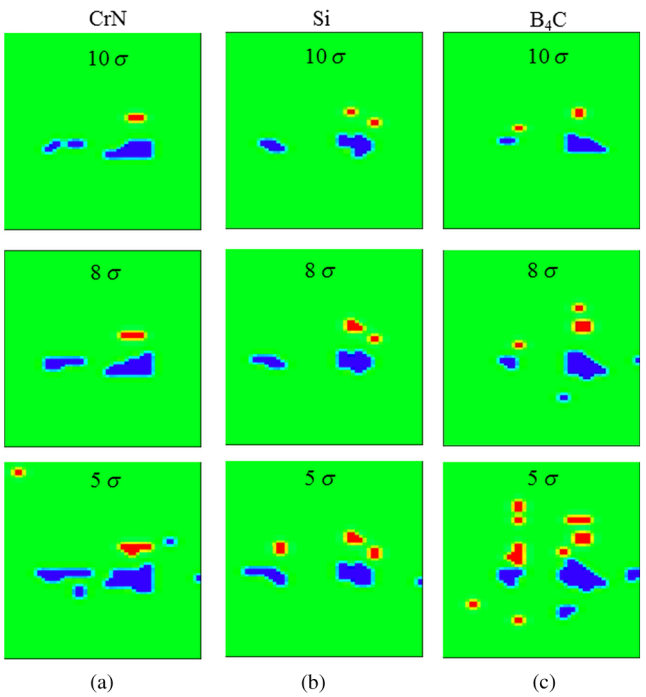

Fig. 9 Simulated difference images using etched 20-pair-ML EUV mask with hp 40 nm L/S pattern on the conductive layers of (a) CrN or TiN, (b) Si, and (c) B_4C with various threshold levels.

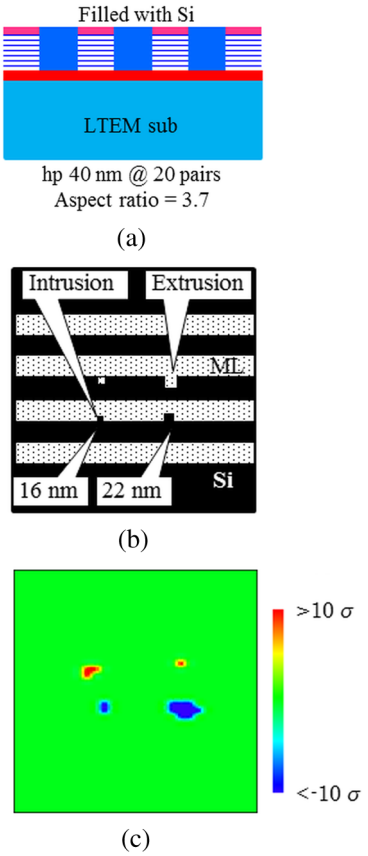

Fig. 10 (a) Cross-sectional and (b) top view of the schematic illustration of the etched 20-pair-ML EUV mask with its spaces filled with Si, and (c) the simulated difference image. The incident beam energy is 600 eV.

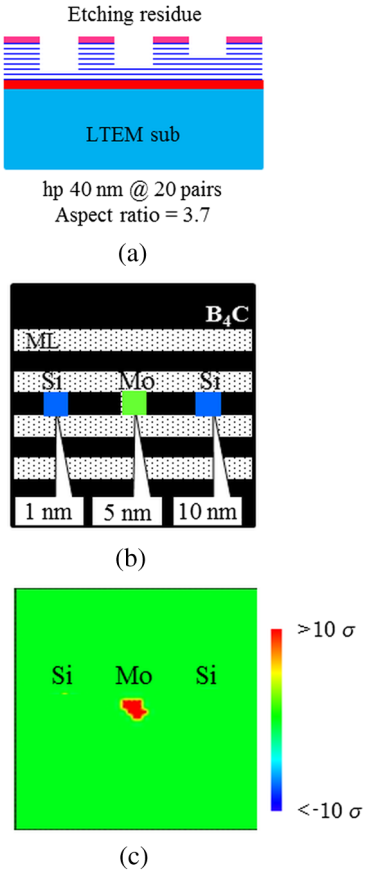

Fig. 11 (a) Cross-sectional and (b) top view of the schematic illustration of the etched 20-pair-ML EUV mask with etching residues, and (c) the simulated difference image on the conductive layers of B_4C. The surfaces of the etching residues with their thicknesses of 1, 5, and 10 nm are covered by Si, Mo, and Si, respectively.

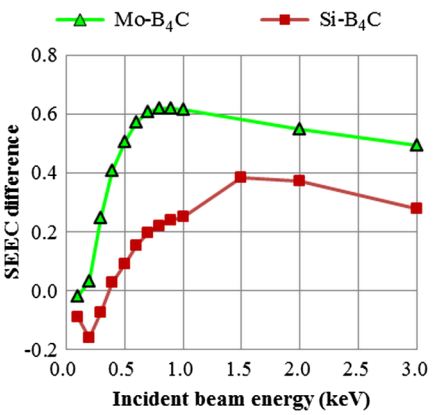

Fig. 12 Experimentally obtained SEEC difference between Mo and B_4C, and between Si and B_4C. The surfaces of Mo and Si are covered by their native oxide.

shift can be explained by using Fig. 4(b). When the surface of Si is leveled with that of the ML, the SEs from the Si reach the detector without being blocked by the sidewalls of the trench [the case of 100% in Fig. 4(b)]. Therefore, the optimal condition is shifted toward the higher energy. It is also noteworthy that the 16-nm-sized extrusion defect is detected in the refilled structure, whereas the same defect is not detected in the Si conductive layer as shown in Fig. 8(b). However, the SEEC difference for the case of 100% (refilled structure) is lower than that of the 80% (40-pair ML as-etched). This phenomenon can be explained by the electron scattering near the edge of the etched ML. In the case of the as-etched structure, strongly scattered electrons near the edge become a source of noise, and they degrade the signal-to-noise ratio (SNR) of the defect signal. On the other hand, in the case of the refilled structure, no such electron scattering is encountered since in this case the surface happens to be flat. Hence, the SNR of the defect signal is improved. A detailed explanation of the phenomena was described earlier.[24]

By using a B_4C conductive layer, a residual-type defect (etching residue)[21,35,36] can also be detected with high sensitivity. However, the sensitivity depends on the surface material of the etching residue as shown in Fig. 11. When the surface of the defect is covered by Mo, only the 5-nm-thick defect is detectable, whereas in the case of Si, even a 10-nm-thick defect cannot be detected. This is because the SEEC difference between Mo and B_4C is much larger than that between Si and B_4C as shown in Fig. 12.

In the case of the real defect, the surface of the defect is often not flat but shows some slopes. Therefore, in most cases, both Mo and Si appear on the defect's surface. Hence, most of the real residual-type defects can be detected.

3.3 *Analysis of Electrical Conductivity and Charging Effect of the Candidate Materials*

In order to investigate the electrical conductivity and surface charging effect of the candidate materials, electrical resistivity and the dependence of beam probe current on the SEEC are evaluated. Table 1 shows the resistivity of the candidate materials with various structures. TiN, CrN, and TaN have good conductivities. In the case of Si, the resistivity of p- or n-type crystal Si is known as 1.0 to 1.0×10^{-2} Ωcm. However, crystal layers are hardly grown on noncrystalline substrates such as quartz and LTEM. Especially for the case of sputtered films, amorphous Si with high resistivity tends to be deposited. On the other hand, B_4C with 100 nm has a comparatively good conductivity, but the electric resistance of 5-nm-thick B_4C film on SiO_2 substrate goes up to an unmeasurable level. From the standpoint of EB repair technique, a resistivity should be as low as possible to demonstrate the precise repair process.[16,17] These results show that an Si conductive layer has a technical problem with depositions onto photomask substrates, and a B_4C film does not seem to be sufficiently conductive to maximize the accuracy

Table 1 Electrical resistivity of the candidate layers (Ωcm).

TiN	CrN	TaN	Doped crystal Si	a-Si	B_4C	B_4C (5 nm)	2.5 nm B_4C on metal film
1.0×10^{-4}	1.4×10^{-4}	2.3×10^{-4}	~1.0	Unmeasurable	23.3	Unmeasurable	$<5.4 \times 10^{-5}$

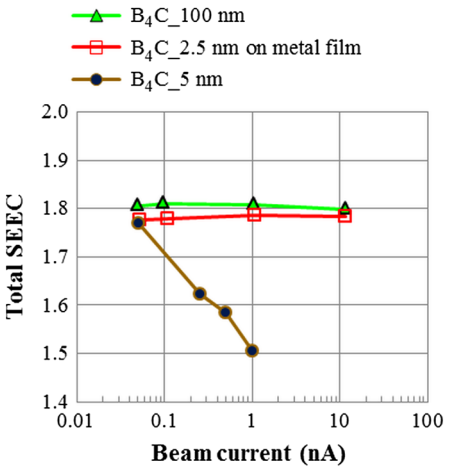

Fig. 13 Experimentally obtained SEECs of 100-nm-thick B_4C film, 2.5-nm-thick B_4C on metal film, and 5-nm-thick B_4C film as functions of primary electron current with a beam energy of 200 eV (the maximum values of their yield curves). Diameter of the focused incident beam was estimated to be ~1.2 μm at 2 nA with 200 eV.

of the repair process and CD metrology, and the sensitivity of pattern inspection. In order to maximize the effect of low SEEC and electrical conductivity, a conductive layer with double-layer structure with 2.5-nm-thick B_4C on metal film is proposed. The resistivity of this type of conductive layer is better than those of TiN, CrN, and TaN. In order to reconfirm the conductivity and investigate the effect of surface charging when the electron beam is irradiated, the dependence of the beam current on the SEEC changes was examined for the three types of B_4C samples as shown in Fig. 13.

The SEECs of 100-nm-thick B_4C film and 2.5-nm-thick B_4C on metal film remain almost constant as the incident electron beam current increases. On the other hand, the SEEC of the 5-nm-thick B_4C film shows a significant decrease with the increasing beam current because the emitted SEs return back to the sample surface due to the strong positive charges involved as shown in Fig. 14.[24,37,38]

When the B_4C film is sufficiently thick, the injected electrons or generated holes can be discharged through the thick B_4C film. However, these charges are stored in the thin B_4C film due to its extreme high resistance. On the other hand, in the case of the double-layer structure, the charges are discharged along with the underlying metal film. We have already reported that the SEEC of the nondoped Si layer with the resistivity of >1000 Ωcm shows a similar decrease along with the increasing beam current, whereas the SEECs of the Ru-capped ML remain almost constant.[24] Moreover, the lateral and vertical conductivities of Ru-capped ML are empirically known to be sufficiently high to avoid any charging effect in spite of 4-nm-thick sputtered Si layers being included.[20] These results indicate that the charging effect attributed to the 2.5-nm-thick B_4C is negligibly small, and the SE signal from the double structured conductive layer is not changed regardless of the electron dosage.

3.4 *Other Items to Be Taken into Account in Selecting the Conductive Layer*

In order to select the conductive layer, the following "other" items are to be taken into account: (1) influence of native

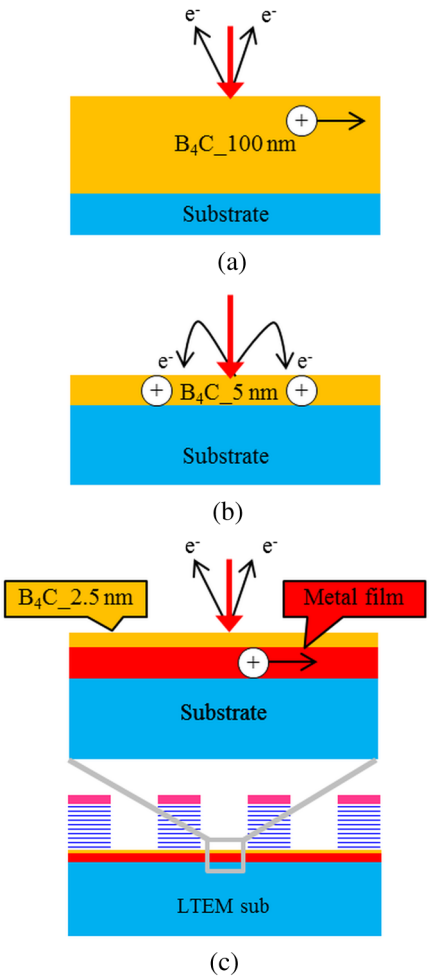

Fig. 14 Schematic explanations of the charging and discharging effects for the samples of: (a) 100-nm-thick B_4C film, (b) 2.5-nm-thick B_4C on metal film, and (c) 5-nm-thick B_4C film.

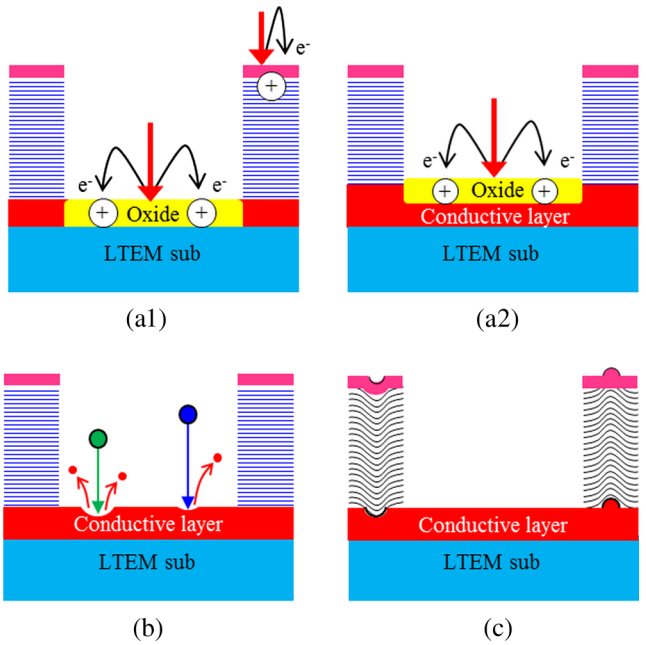

Fig. 15 Schematic explanations of (a1) and (a2) influence of native oxide, (b) etching selectivity, and (c) phase defects.

oxide, (2) etching selectivity, and (3) additional phase defects.

i. If the native oxide is thicker than the conductive layer, patterns become electrically floating as shown in Fig. 15(a1). On the other hand, if the native oxide is thinner than the conductive layer, the native oxide does not affect the mask conductivity but does affect the surface charging as shown in Fig. 15(a2). However, if the metal film is capped by B_4C, the conductive layer is not affected by the native oxide.[28] Hence, the question of native oxide can be resolved by using the double-layer structure with 2.5-nm-thick B_4C on metal film.

ii. The conductive layer should play the role of an etch stop layer of a dry etch process. The ML is composed of Si and Mo; therefore, Si is not adequate for the conductive layer from the standpoint of etching selectivity as shown in Fig. 15(b). B_4C is known as a very stable component and has strong chemical and mechanical resistance.[28] However, the etching selectivity against ML should be confirmed, or the appropriate etching condition should be studied.

iii. Additional phase defects derived from the conductive layer should be suppressed. The phase defect is one of the issues to be addressed on EUV masks.[39,40] Pit or bump defects on the mask substrate, and particles attached before and during the deposition process of ML, are the origins of phase defects as shown in Fig. 15(c). The influence of the conductive layer on the increase or decrease of phase defect should be investigated.

4 Summary and Conclusions

Patterned mask inspection for an etched ML-EUV mask was investigated. In order to optimize the mask structure not only from the standpoint of a pattern inspection using PEM but also considering other fabrication processes using EB technique such as CD metrology and mask repair, we focus on a conductive layer between the ML and substrate. Candidate materials to serve as the conductive layer were selected from the familiar materials used in photomasks, such as TaN, Ru, CrN, TiN, Si, and B_4C. By measuring the SEECs of the candidate materials for the conductive layer, the combination of B_4C conductive layer and Ru-capped ML was found to have the best pattern image contrast due to its highest SEEC difference. In the cases of 40-pair ML, 16-nm-sized extrusion and intrusion defects were found to be detectable more than 10σ in hp 44, 40, and 32 nm L/S patterns. Although reduction of 40-pair ML to 20-pair ML degraded the image contrast and the defect detectability, 16-nm-sized defects remained detectable in the case of B_4C sample. These defects were detected after the etched part was refilled with Si. Moreover, the simulation shows a high sensitivity for detecting the residual-type defects (etching residues). In order to maximize the effect of low SEEC and electrical conductivity, a double-layer structured conductive layer with 2.5-nm-thick B_4C on metal film was proposed. This conductive layer was found to have sufficient conductivity ($<5.4 \times 10^{-5}$ Ωcm) and also was found to be free from the surface charging effect and any influence of native oxide.

Acknowledgments

The authors would like to thank T. Kamo, K. Takai, M. Naka, R. Yoshikawa, S. Kanamitsu, and T. Hirano of Toshiba Corporation for useful discussions. This work was supported by the New Energy and Industrial Technology Development Organization.

References

1. B. Kneer et al., "EUV lithography optics for sub-9nm resolution," *Proc. SPIE* **9422**, 94221G (2015).
2. J. T. Neumann et al., "Interactions of 3D mask effects and NA in EUV lithography," *Proc. SPIE* **8522**, 852211 (2012).
3. B. La Fontaine et al., "Architectural choices for EUV lithography masks: patterned absorbers and patterned reflectors," *Proc. SPIE* **5374**, 300 (2004).
4. T. Schmoeller et al., "The impact of mask design on EUV imaging," *Proc. SPIE* **7379**, 73792H (2009).
5. C. Chovino et al., "EUV mask making: an approach based on the direct patterning of the EUV reflector," *Proc. SPIE* **5256**, 566 (2003).
6. K. Takai et al., "Patterning of EUVL binary etched multilayer mask," *Proc. SPIE* **8880**, 88802M (2013).
7. G. J. Kim et al., "Etched multilayer mask is better than conventional absorber mask," *Proc. SPIE* **9256**, 92560R (2014).
8. G. J. Kim et al., "Etched multilayer mask in EUV lithography for 16 nm node and below," *Proc. SPIE* **9256**, 92560Q (2014).
9. S. Yamaguchi et al., "Performance of EBeyeM for EUV mask inspection," *Proc. SPIE* **8166**, 81662F (2011).
10. T. Shimomura et al., "Electron beam inspection of 16 nm hp node EUV masks," *Proc. SPIE* **8522**, 85220L (2012).
11. R. Hirano et al., "Development of extreme ultraviolet mask pattern inspection technology using projection electron beam optics," *J. Micro/Nanolith. MEMS MOEMS* **12**, 021003 (2013).
12. R. Hirano et al., "Patterned mask inspection technology with projection electron microscope technique on extreme ultraviolet masks," *J. Micro/Nanolith. MEMS MOEMS* **13**, 013009 (2014).
13. S. Iida et al., "Dependence of defect size and shape on detectability for EUV patterned mask inspection," *Proc. SPIE* **9422**, 942225 (2015).
14. Y. Nishiyama et al., "Influence of the charging effect on the precision of measuring EUV mask features," *Proc. SPIE* **7971**, 79710C (2011).
15. S. Babin et al., "CD-metrology of EUV masks in the presence of charging: measurement and simulation," *Proc. SPIE* **8441**, 844108 (2012).
16. S. Kanamitsu, T. Hirano, and O. Suga, "Prospect of EUV mask repair technology using e-beam tool," *Proc. SPIE* **7823**, 782322 (2010).
17. S. Kanamitsu, K. Morishita, and T. Hirano, "Application of EB repair for high durable MoSi PSM," *Proc. SPIE* **9256**, 92560U (2014).
18. U. Dietze et al., "Effective EUVL mask cleaning technology solutions for mask manufacturing and in-fab mask maintenance," *Proc. SPIE* **7985**, 79850N (2011).
19. K. Takai et al., "Capability of etched multilayer EUV mask fabrication," *Proc. SPIE* **9235**, 923515 (2014).
20. K. Takai et al., "Improvement of EUVL mask structure with black border of etched multilayer," *Proc. SPIE* **8701**, 87010Y (2013).
21. S. Iida et al., "Identification of residual-type defect on extreme ultraviolet mask by projection electron microscope using Monte Carlo simulation," *J. Vac. Sci. Technol. B* **30**, 06F503 (2012).
22. S. Iida et al., "Extreme ultraviolet mask defect inspection with a half pitch 16-nm node using simulated projection electron microscope images," *J. Micro/Nanolith. MEMS MOEMS* **12**, 023013 (2013).
23. S. Iida et al., "Impact of electron scattering in extreme ultraviolet reflective multilayer on electron image," *J. Vac. Sci. Technol. B* **31**(6), 06F601 (2013).
24. S. Iida et al., "Impact of B_4C capping layer for extreme ultraviolet mask on the sensitivity of patterned mask inspection using a projection electron microscope," *J. Micro/Nanolith. MEMS MOEMS* **13**, 043015 (2014).
25. S. Iida et al., "Simulation technique for pattern inspection using a projection electron microscope," *J. Vac. Sci. Technol. B* **33**(6), 06FN02 (2015).
26. S. Iida et al., "Analysis of image distortion on projection microscope image," *Jpn. J. Appl. Phys.* **53**, 116602 (2014).
27. S. Bajt et al., "Improved reflectance and stability of Mo/Si multilayers," *Opt. Eng.* **41**, 1797 (2002).
28. I. Y. Jang et al., "Ruthenium (Ru) peeling and predicting robustness of the capping layer using finite element method (FEM) modeling," *Proc. SPIE* **9256**, 92560I (2014).
29. M. Kadowaki et al., "Investigation of factors causing difference between simulation and real SEM image," *Proc. SPIE* **7272**, 72723I (2009).
30. S. Babin et al., "CHARIOT: software tool for modeling SEM signal and e-beam lithography," *Phys. Procedia* **1**, 305 (2008).
31. H. Watanabe et al., "EUV patterned mask inspection system using a projection electron microscope technique," *Proc. SPIE* **8880**, 88800U (2013).

32. Y. Lin and D. C. Joy, "A new examination of secondary electron yield data," *Surf. Interface Anal.* **37**, 895 (2005).
33. D. Bizen, Y. Sohda, and H. Kazumi, "Dependence of secondary-electron yield on aspect ratio of several trench patterns," *Proc. SPIE* **9050**, 90500K (2014).
34. R. Hirano et al., "Extreme ultraviolet lithography patterned mask defect detection performance evaluation toward 16- to 11-nm half-pitch generation," *J. Micro/Nanolith. MEMS MOEMS* **14**, 033512 (2015).
35. T. Amano et al., "Residual-type mask defect printability for extreme ultraviolet lithography," *J. Vac. Sci. Technol. B* **30**(6), 06F501 (2012).
36. T. Amano et al., "Observation of residual-type thin absorber defect on extreme ultraviolet lithography mask using an extreme ultraviolet microscope," *Appl. Phys. Express* **6**, 046501 (2013).
37. S. Aoyagi and K. Ura, "Initialization by erasing the surface potential of negatively charged insulators in scanning electron microscope (SEM) observation," *J. Electron Microsc.* **48**, 555 (1999).
38. M. Miyoshi and K. Ura, "Negative charging-up contrast formation of multilayered structures with a nonpenetrating electron beam in scanning-electron microscope," *J. Vac. Sci. Technol. B* **23**, 2763 (2005).
39. T. Amano and T. Terasawa, "Propagation of surface topography of extreme ultraviolet blank substrate through multilayer and impact of phase defect structure on wafer image," *J. Micro/Nanolith. MEMS MOEMS* **12**, 033015 (2013).
40. T. Harada et al., "Phase defect characterization on an extreme-ultraviolet blank mask using microcoherent extreme-ultraviolet scatterometry microscope," *J. Vac. Sci. Technol. B* **31**, 06F605 (2013).

Susumu Iida received his BS and MS degrees in 1995 and 1997, respectively, and in 2000, he earned his PhD in electronics, all from Shizuoka University, Japan. He joined the Research and Development Center at Toshiba Corporation. In 2011, he was assigned to EIDEC, and since then he has been engaged in the development of patterned mask inspection.